Measurement of Ion Temperature and Toroidal Rotation Velocity Using Charge Exchange Recombination Spectroscopy in Heliotron J

Hyunyong LEE, Shinji KOBAYASHI[1)], Takayuki MINAMI, Shinichiro KADO[2)], Tohru MIZUUCHI[1)], Kazunobu NAGASAKI[1)], Hiroyuki OKADA[1)], Takashi MINAMI[1)], Satoshi YAMAMOTO[1)], Sadayoshi MURAKAMI[3)], Yuji NAKAMURA, Kiyoshi HANATANI[1)], Shigeru KONOSHIMA, Shinsuke OHSHIMA[4)], Kiyofumi MUKAI, Tasuku KAGAWA and Fumimichi SANO[1)]

Graduate School of Energy Science, Kyoto University, Uji, Kyoto, 611-011, Japan
[1)]*Institute of Advanced Energy, Kyoto University, Uji, Kyoto, 611-011, Japan*
[2)]*Graduate School of Engineering, University of Tokyo, Bunkyo, Tokyo, 113-8656, Japan*
[3)]*Graduate School of Engineering, Kyoto University, Yoshida, Kyoto, 606-8501, Japan*
[4)]*Pioneering Research Unit for Next Generation, Kyoto University, Uji, Kyoto, 611-011, Japan*

(Received 2 August 2011 / Accepted 23 January 2012)

This paper describes design and installation of a charge-exchange recombination spectroscopy (CXRS) system in Heliotron J. In this system, two tangential-heating neutral beams are used for plasma heating as well as the diagnostic beams. The sightlines are set to be parallel to the magnetic axis to achieve high spatial resolution. The spatial resolution is $\Delta\langle r/a\rangle \sim 0.05$ for a measurement area of $0.37 < \langle r/a\rangle < 0.79$. We adopted a Czerny-Turner monochromator, whose dispersion is 0.74 nm/mm. We applied this system is applied to an NBI plasma and the time evolution of the ion temperature and the toroidal rotation velocity profile are successfully obtained.

Keywords: ion temperature, toroidal rotation velocity, CXRS, NBI, Heliotron J

DOI: 10.1585/pfr.7.1402019

1. Introduction

Measurement of ion temperature (T_i) and plasma rotation velocity (v_ϕ, v_θ) profiles is important to understand the ion thermal and momentum transport phenomena in magnetically confined plasmas. Moreover, it is also important to investigate the spontaneous rotation for a fusion reactor, such as ITER, since the expected external torque injection is not enough to stabilize the MHD instabilities [1]. A charge-exchange recombination spectroscopy (CXRS) method is a useful diagnostic to measure the ion temperature and rotation velocity profiles and has been performed in Tokamaks, such as JT-60U [2], DIII-D [3] and JET [4], and in Stellarators/Heliotrons, such as LHD [5,6], W7-AS [7] and TJ-II [8]. This method is to measure an emission from charge-exchange recombination reactions between fully ionized impurity ions (A^{z+}) and energetic hydrogen atoms of the neutral beam (H^0) as follows:

$$\mathrm{H}^0 + \mathrm{A}^{z+} \rightarrow \mathrm{H}^+ + \mathrm{A}^{(z-1)+}(n, l)$$

where (n, l) refers to an excited state of $\mathrm{A}^{(z-1)+}$ with subsequent photon emissions. The ion temperature and rotation velocity are estimated from the Doppler broadening and the Doppler shift, respectively, of the spectral line. A CXRS method can realize a good spatial resolution and allow time-resolved ion temperature and rotation velocity profiles in a single shot [3].

In Heliotron J, T_i has been measured using a neutral particle analyzer (NPA) [9] but the rotation velocity has not been measured. Since NPA has an integral effect along its sightline, it is not suited to local measurements of T_i. To investigate local transport phenomena, measurement of T_i and v_ϕ profiles is necessary. Therefore, we have installed a CXRS system in Heliotron J to measure T_i and v_ϕ profiles.

In this paper, first, we introduce the CXRS system, which is installed in Heliotron J, in Chapter 2. In Chapter 3, we describe the several calibrations to measure measurement on T_i and v_ϕ accurately. The first results of T_i and v_ϕ profiles measurement in Heliotron J are reported in Chapter 4. Finally, we summarize our results in Chapter 5.

2. Charge Exchange Recombination Spectroscopy System in Heliotron J

Figure 1 shows heating devices, gas fuelling systems and certain diagnostic systems in Heliotron J. Heliotron J is a helical-axis heliotron device with an $L/M = 1/4$ helical coil, where L is the pole number and M is the helical pitch of the helical coil [10, 11]. Two tangential neutral beam lines (BL1, BL2) with positive ion sources (maximum acceleration voltage is 30 kV, maximum port through

author's e-mail: lee-hy@center.iae.kyoto-u.ac.jp

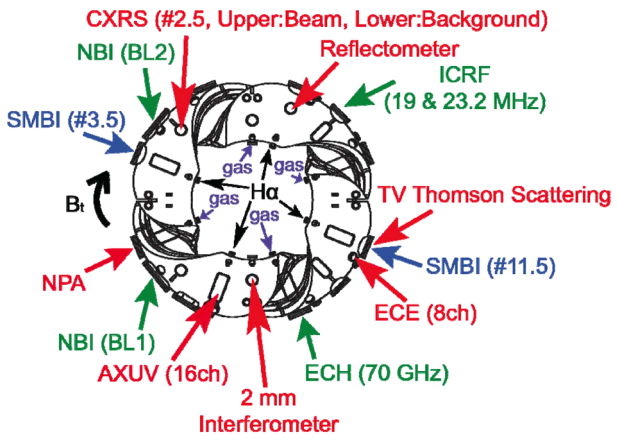

Fig. 1 Heating devices, gas fuelling system and diagnostics in Heliotron J.

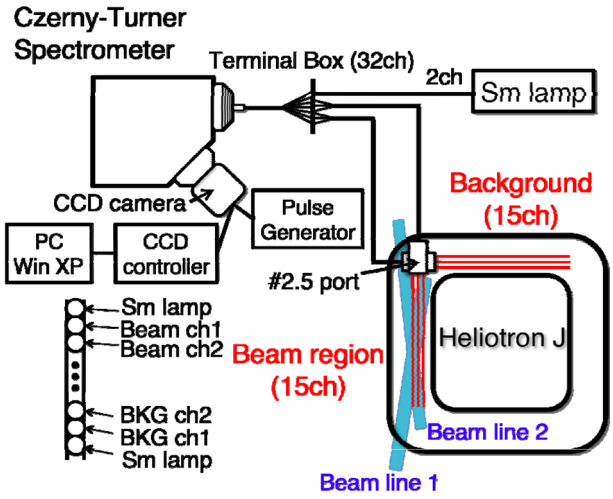

Fig. 2 CXRS system in Heliotron J.

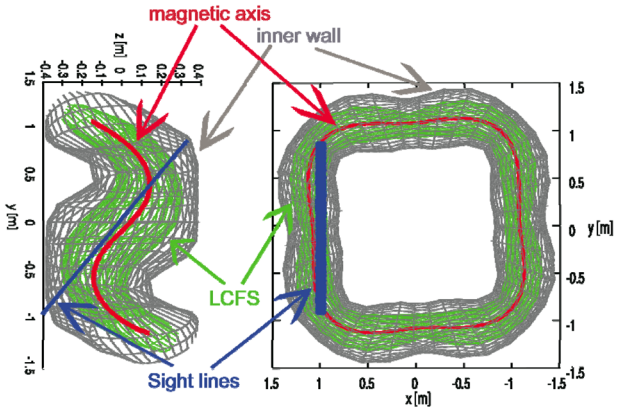

Fig. 3 Schematic view of the designed CXRS sightlines in Heliotron J.

injection power is 800 kW on the each beam line) are used for plasma heating. One is co-direction (BL2) and the other is counter injection (BL1) for the normal direction of the magnetic field. Here, the co direction is defined as the direction of the plasma current, which increases the rotational transform. These beams are also used as diagnostic beams for CXRS. A gas puffing (GP) system and two super molecular beam injection (SMBI) systems are installed for the fuelling. The SMBI is an effective gas fuelling technique, which can penetrate its fuelling gas deeper into the plasma compared to the normal gas-puffing [12]. The line-averaged electron density is measured by using a 2 mm interferometer. The NPA system is equipped to measure T_i and the fast ion distribution in both velocity and real spaces.

Figure 2 shows the CXRS system in Heliotron J. This system measures the CVI line (n = 7-8, 529.05 nm). We install two sets of optical fibers (beam and background region) to remove the cold component, which is an emission from excitation via electron impact and charge-exchange with thermal neutral. Two sets of optical fibers are adopted to be symmetrical against toroidal direction. Each optical set has 15 sightlines. The objective lenses are arranged to focus the CXR emission into the optical fibers, whose numerical aperture (NA) is 0.2 and core diameter is 0.2 mm. We installed a Czerny-Turner monochromator, whose F number is 2.8, focal length is 400 mm, grating is 2160 grooves/mm and γ, which is the half angle between the incident optical axis and output optical axis, is 15 degree. A camera with back-illuminated charge coupled device (ANDOR DU-887, 512×512 pix, 16 μm^2/pix, and maximum scanning frequency = 400 Hz), is mounted on the monochromator. The scanning is externally triggered by a pulse generator.

The magnetic configuration of Heliotron J has a three-dimensional structure. To obtain a high spatial resolution using the tangential-heating neutral beams, we choose the sightlines of the CXRS system parallel to the magnetic axis. In this case, the spatial resolution of each sightline can be small [13]. Figure 3 schematically shows the top- and side-views of the designed CXRS sightlines, including the inner wall surface of the vacuum vessel, last closed flux surface (LCFS) and magnetic axis. Heliotron J has a three-dimensional magnetic axis, which has a square shape at the top view and a sinusoidal shape at the side view. Figure 4 shows the normalized minor plasma radius ($\langle r/a \rangle$) along each sightline as a function of the distance from a pivot point (#2.5 port, see Figs. 1 and 2) under the standard magnetic configuration. Here, the pivot point represents the location of a reflection mirror. Since, the neutral beams cross the sight lines at approximately 0.7 ~ 1.3 m from the pivot point (see Fig. 4), each sightline effectively correspond to a value of $\langle r/a \rangle$ with a small deviation. Therefore, we expect to achieve high a spatial resolution.

The measurement location in $\langle r/a \rangle$ and the spatial resolution are evaluated from the CXR emissivity calculation. The CXR emissivity, which has a sightline dl, can be estimated by the following equation,

$$I_{CXR} \propto \int n_{imp} n_{beam} \sigma_{CXR} |v| \, d\omega \, dl, \quad (1)$$

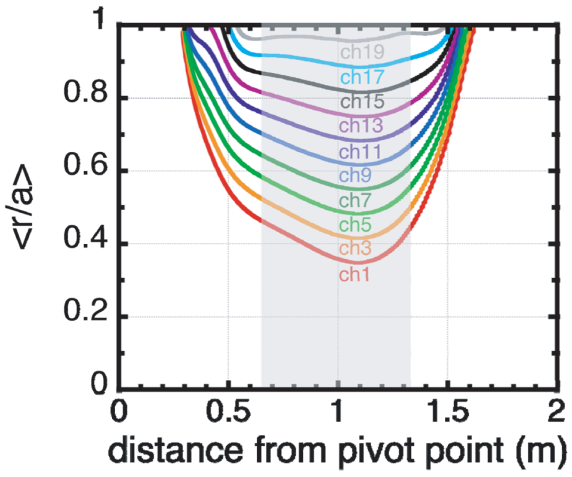

Fig. 4 Normalized minor radius ($\langle r/a \rangle$) of plasma along each sightline as a function of the distance from a pivot point (#2.5 port, see Fig. 2) under the standard magnetic configuration [13].

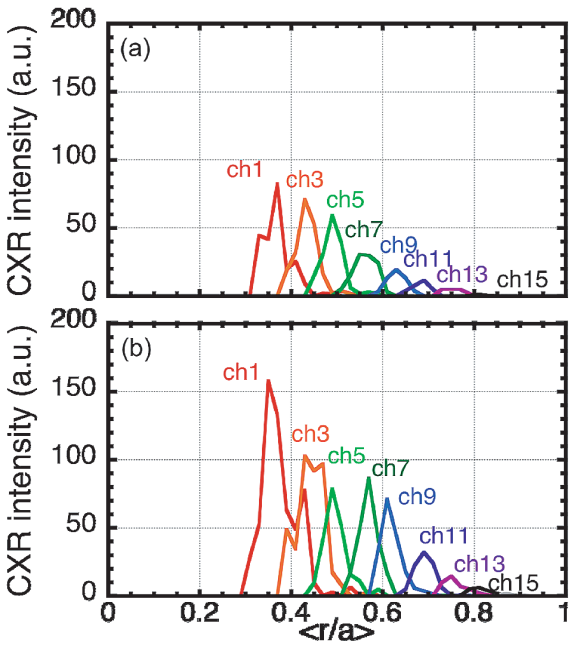

Fig. 5 Radial profile of CXR emissivity on each channel for BL1 (a) and BL2 (b).

where n_{imp}, n_{beam}, σ_{CXR}, $|v|$ and $\mathrm{d}\omega$ denote the impurity ion density, neutral beam density, charge exchange cross section between the impurity ions and a neutral particles by NBI, the relative velocity, and the solid angle at the CXR emission respectively. In the calculation, the peaked density profile of the impurity ion (C^{6+}) is assumed to be proportional to $((1-\rho^2)^3)$. The neutral beam is estimated from the neutral beam trajectory based on a Monte-Carlo simulation for the beam birth-point analysis [14]. We used the ADAS [15] data for computing σ_{CXR}. The relative velocity is assumed to be the acceleration velocity of NBI. The bulk ion temperature (several hundred eV), which was measured with the NPA, is much smaller than the acceleration voltage of NBI [13]. The calculation for BL2 is reported in [13], and the same calculation is also applied to BL1. Figure 5 shows the expected radial profiles of CXR emissivity for each channel under the standard magnetic configuration (Figs. 5 (a) and 4 (b) for BL1 for BL2, respectively). Here, the acceleration voltage of NBI is 24 kV. We fit a Gaussian function to these profiles to estimate the measurement location and the spatial resolution. The measurement location is defined as the mean value of the Gaussian distribution function and the spatial resolution is defined as its variance value of Gaussian distribution function. Figure 6 shows the measurement area and the spatial resolution for each sightline (chord number). The measurement area is $0.37 < \langle r/a \rangle < 0.79$ for BL2 and $0.38 < \langle r/a \rangle < 0.79$ for BL1 in normal magnetic field. The spatial resolution ($\Delta\langle r/a \rangle$) is about 0.05 in the measurement area for the two cases.

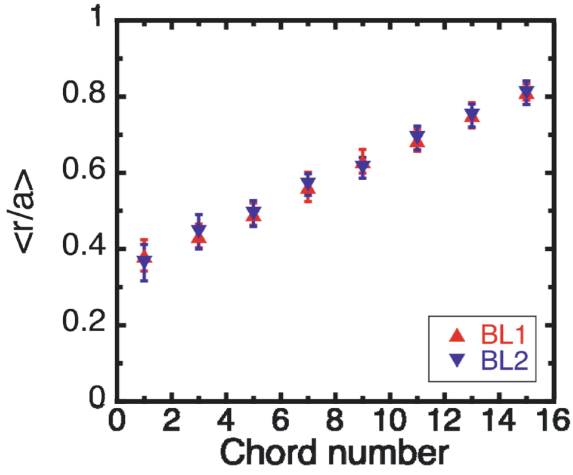

Fig. 6 Measurement location and spatial resolution for each sightline.

3. Calibration

Several calibrations are necessary to accurately estimate T_{i} and v_ϕ. The instrument function of monochromator and the fine structure of the transition spectrum could affect to estimate T_{i}. To evaluate the Doppler shift, identification of the accurate position of λ_0 (529.05 nm) on an image of CCD camera is necessary. In addition, the dispersion of monochoromator must be measured. Therefore, we experimentally confirmed the dispersion and the instrument function of the Czerny-Turner monochromator, and the λ_0 position on the CCD image. The effect of the fine structure on T_{i} was studied based on a numerical calculation.

Figures 7 (a) and 7 (b) show the experimentally obtained dispersion and instrument function of the Czerny-Turner monochromator, respectively. The dispersion is

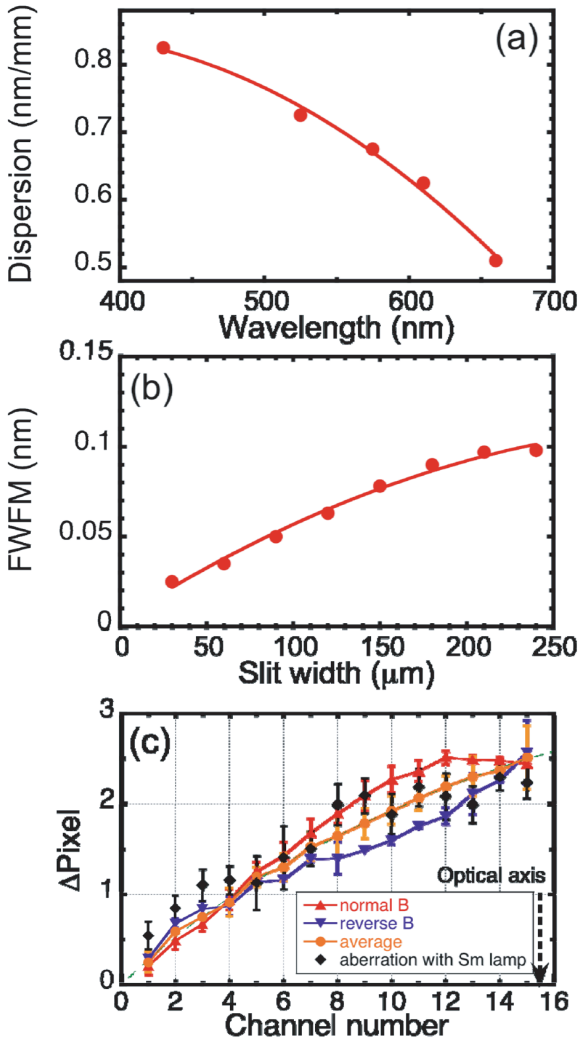

Fig. 7 (a) Dispersion of the Czerny-Turner monochromator, (b) Instrument function of Czerny- Turner monochromator as a function of the slit width, (c) Shift of λ_0 positions on the CCD image.

about 0.74 nm/mm, corresponds to 1.2×10^{-2} nm/pix at 529.05 nm. We measured the instrument function by changing the slit width from 0 μm to 250 μm. For measurement, the slit width is set to 100 μm, so that the instrument function is approximately 0.05 nm.

To estimate the rotation velocity, the λ_0 position (529.05 nm) for each channel must be accurately determined on the CCD images. Because, the objective lenses are installed in front of the CCD camera for focusing, the lens aberration affects the λ_0 position for each channel. We estimated the λ_0 position, which is considered lens aberration measured with a line emission (527.14 nm) from an Sm lamp, for each channel on the CCD images. The black dots in Fig. 7 (c) denote the λ_0 positions considered to lens aberration for each channel We determined the λ_0 position by fitting the measured Sm lamp spectral profile to an ideal Gaussian function via the nonlinear Marquardt's least-squares method. The error bars are estimated from the uncertainties in the Gaussian fit parameters [16]. To check the accuracy of λ_0 positions, we measured the Doppler shift from the λ_0 position in electron cyclotron heating (ECH) plasmas (quasi-steady-state discharges with a line averaged electron density of 0.6×10^{19} m^{-3}) in the normal and reversed magnetic fields. The observed shift includes the lens aberration effect and the Doppler shift due to the toroidal rotation of cold component. If the change in the field direction reverses completely, we can cancel out the Doppler shift effect due to the toroidal rotation of cold component by taking the averaged value of the observed shifts between the two cases. The Doppler shift from the λ_0 position is determined by fitting the measured spectral profile to an ideal Gaussian fit via the nonlinear Marquardt's least square method. The error bars are estimated from the uncertainties in the Gaussian fit parameters [16].

In Fig. 7 (c), the red and blue lines denote the observed shifts on each channel in the normal and reverse magnetic fields, respectively, and the orange line denotes the averaged of theses shifts between them. Here, the optical axis is projected on between the channel 15 and 16. The differences in λ_0 positions are proportional to y^2, where y is the distance from the optical axis. The λ_0 positions evaluated with both methods agree well.

The fine structure components influence the T_i evaluation. Figure 8 (a) shows the fine structure components of the CVI Δn = 7-8 transition at T_i = 0 eV. The relative intensities of each component are obtained from the cascade-corrected transition coefficient and population including l mixing in higher n states [3]. The population of each j level of the upper states was estimated by the cascade-corrected l distribution and the Buger-Dorgelo-Oristein sum rule [17]. Here, we assume that all transitions are under the ground state. If T_i is not 0 eV, each component has the Doppler broadening. The sum of each component will be an actual measured spectral profile, resulting wider broadening expected from T_i. Therefore, we should consider this difference between the real T_i and the apparent T_i. Figure 8 (b) shows the correction factor between the real T_i and the apparent T_i, which is observed T_i. The correction factor is estimated from the ratio of full width at half maximum (FWHM), which is considered the instrument function by taking the convolution between each FWHM and the instrument function. The FWHM of a Gaussian shape, W, is given by

$$W = 1.73\times10^{-3}\times\lambda\left(\frac{T_i}{z}\right)^{\frac{1}{2}}, \quad (2)$$

where λ is the transition wavelength. The correction factor increases from 0.8 to 0.95 as T_i increases from 100 eV to 1000 eV.

Additionally, sensitivities between two optical sets should be checked. Therefore, we carried out the sensitivity calibration in an ECH plasma. We measured emission intensities and calculated ratio between emissions measured by two sets of optical fibers. These ratios are multi-

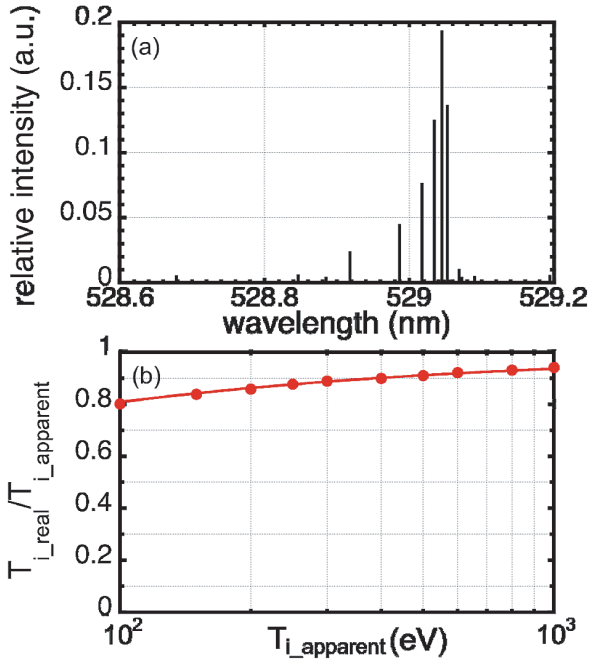

Fig. 8 (a) Fine structure components of the CVI Δn = 7-8 transition at T_i = 0 eV, (b) Correction factors for T_i.

plied to the signal of cold component.

4. First Result of Ion Temperature and Toroidal Rotation Velocity Measurement in NBI Plasmas

In this chapter, we present the first result on T_i and v_ϕ profiles in NBI plasmas of Heliotron J. Figure 9 shows the time evolutions of several plasma parameters in NBI plasmas with SMBI. The ECH was used to generate the plasma from 160 ms to 170 ms and its injection power was about 270 kW. The counter-NBI is injected from 170 ms to 270 ms and the co-NBI is additionally injected from 220 ms to 270 ms. Here, the total port through power is about 1 MW (co-NB : 500 kW, counter-NB : 500 kW). Gas fuelling by GP is performed from 160 ms to 240 ms and a single pulse of SMBI is applied at 215 ms from port #3.5, which is indicated as a spike like signal of Hα 3.5 in Figs. 9 (b). The line-averaged electron density of the plasma is jumped up by SMBI from 1.8×10^{19} m^{-3} to 2.6×10^{19} m^{-3} and then gradually increases up to more than 3.0×10^{19} m^{-3}. The stored energy decreased just after SMBI, and then increased up to 3.8 kJ. Figures 9 (c), (d), and (e) show the time evolution of the CXR emission intensity, T_i, and v_ϕ, respectively. The scanning frequency of the CCD camera is 100 Hz in this discharge. The ion temperature and toroidal rotation velocity are determined by fitting the measured spectral profile with an ideal Gaussian function via the nonlinear Marquardt's least-squares method. The error bars are estimated from the uncertainties in the Gaussian fit parameters [16].

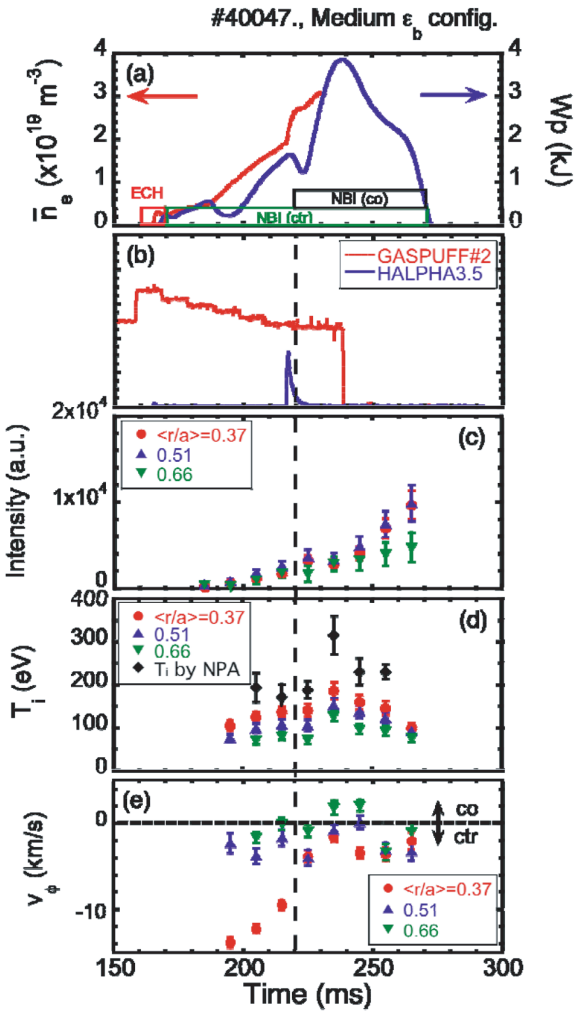

Fig. 9 Time evolution of (a) line-averaged electron density and the stored energy, (b) signal of gas puffing and the intensity of Hα at #3.5 (c) CXR emission intensity, (d) ion temperature, and (e) toroidal rotation velocity.

The CXR emission intensity increases during discharge. The ion temperature at 235 ms is greater than that at $t < 225$ ms. The ion temperature reached its maximum when the stored energy came to the maximum. The increase of T_i (about 100 eV) measured with NPA, whose sightline crosses the magnetic axis, is larger than that measured with CXRS ($0.37 < \langle r/a \rangle < 0.79$, about 50 eV). This suggests that T_i near the plasma center increases larger than that near the plasma periphery. The toroidal rotation velocity at $\langle r/a \rangle = 0.37$ slows down in the counter direction from about 12 km/s at 205 ms to about 2 km/s at 235 ms.

Figure 10 shows T_i and v_ϕ profiles at 215 ms, when the plasma is sustained only by the counter-NB, and 235 ms, when the plasma is sustained by the co- and the counter-NBs and the stored energy was maximum. The increase of ion temperature in the region of $0.37 < \langle r/a \rangle < 0.79$ is ~ 20-40 eV and those shapes of radial profile are almost same at 215 and 235 ms. At t = 215 ms, the toroidal rotation velocity changes along the minor radius from ~ 10 km/s in

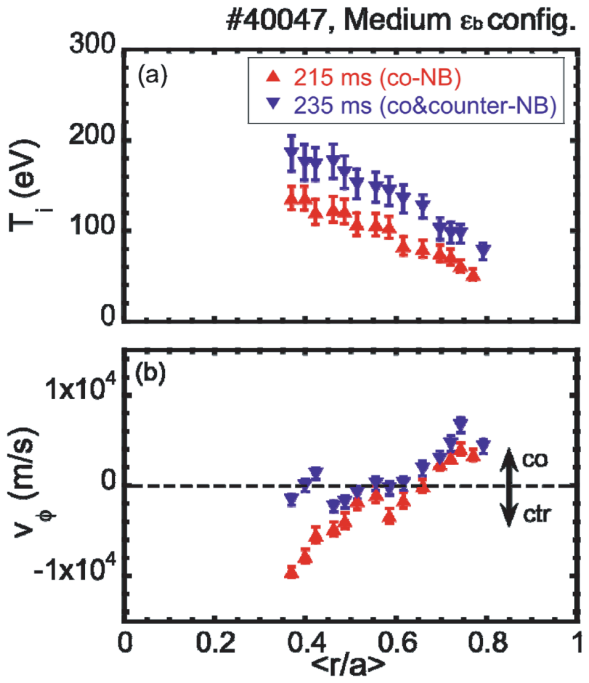

Fig. 10 Radial profiles of (a) ion temperature and (b) toroidal rotation velocity at t = 215 and 235 ms.

the counter direction at $\langle r/a \rangle = 0.37$ to ~ 4 km/s in the co direction at $\langle r/a \rangle = 0.79$. At $t = 235$ ms, the toroidal rotation velocity slows down to about 0 km/s in the region of $0.37 < \langle r/a \rangle < 0.43$. The decreasing rate of v_ϕ in the region of $0.37 < \langle r/a \rangle < 0.43$ is about twice larger than that in the region of $0.43 < \langle r/a \rangle < 0.6$. The observed reduction of v_ϕ in the region of $0.37 < \langle r/a \rangle < 0.43$, might be caused by the additional co-NB. However, note that v_ϕ at $\langle r/a \rangle = 0.37$ starts decreasing with the increasing electron density before the injection of co-NB (see Figs. 9 (a) and (e)). This suggests that the electron density effect on the reduction of v_ϕ in this region. To clarify the origin of the reduction of v_ϕ in this region, the measurement of the electron density profile is necessary. At $\langle r/a \rangle = 0.66 \sim 0.79$, on the other hands, the toroidal rotation velocity increases slightly from 205 ms in the co direction. In the plasma periphery, the external torque due to NB should be smaller than those in the plasma center. Therefore, the change of toroidal rotation in the periphery region might be the change of spontaneous flow. However, to clarify the origin of the observed toroidal flow, we must estimate the external torque injection profile by NB and neoclassical parallel viscosity with experimentally measured electron density and temperature profile.

5. Summary

The high spatial resolved CXRS system is designed by using two tangential-heating neutral beams as the diagnostic beams, and installed in Heliotron J. We achieved a wide measurement area of about $0.37 < \langle r/a \rangle < 0.79$ and a high spatial resolution of $\Delta\langle r/a \rangle \sim 0.05$ simultaneously by the selecting the sightlines parallel to the magnetic axis. The spectral resolution is 0.74 nm/mm by adopting the Czerny-Turner monochromator. The experimentally measured instrument function is 0.05 nm when the slit width is set to 100 μm. To estimate v_ϕ accurately, the lens aberration effect is considered to determine the λ_0 position (529.05 nm) on the CCD images. The correction factor of T_i is calculated for the apparent spectral broadening effect due to the fine structure of the transition. It is in the range of 0.8 ~ 0.95 for T_i of 100 ~ 1000 eV.

By using this CXRS system, the ion temperature and toroidal rotation velocity profiles are measured in a set of NBI plasma. The ion temperature measured by CXRS reaches its maximum when the stored energy reaches to maximum. From the comparison to the NPA measurements, it is suggested that the T_i close to the plasma center increases larger than that close to the plasma periphery. As for the toroidal rotation velocity, we successfully observed the changes in its radial and temporal profile. To understand the observed behavior of the ion temperature and the toroidal rotation velocity profiles, it is necessary to extend the measurement area to plasma center ($\langle r/a \rangle < 0.37$) in addition to the studies of the external torque injection profile by each NB and neoclassical parallel viscosity.

Acknowledgments

Authors are grateful for the great support of the Heliotron J technical staff. This work was partially supported by NIFS collaborative research program (NIF10KUHLLL030, NIFS09KUHL025, etc) and the GCOE program in Kyoto University. This work was also partially funded by the Grants-in-Aid for Scientific Research (Kiban (c) 21560857) and for Young Scientists (Wakate (A) 20686061), MEXT.

[1] D.J. Ward *et al.*, Phys. Plasmas **2**, 1570 (1995).
[2] Y. Koide *et al.*, Rev. Sci. Instrum. **72**, 1 (2001).
[3] R.J. Fonck *et al.*, Phys. Rev. A **29**, 6 (1984).
[4] M.G. Hellermann *et al.*, Rev. Sci. Instrum. **61**, 11 (1990).
[5] K. Ida *et al.*, Rev. Sci. Instrum. **71**, 6 (2000).
[6] M. Yoshinuma *et al.*, Plasma Fusion Res. **3**, S1014 (2008).
[7] J. Baldzuhn *et al.*, Rev. Sci. Instrum. **68**, 1020 (1997).
[8] J.M. Carmona *et al.*, Rev. Sci. Instrum. **77**, 10F107-1 (2006).
[9] M. Kaneko *et al.*, J. Plasma Fusion Res. SERIES **7**, 77 (2006).
[10] M. Wakatani *et al.*, Nucl. Fusion **40**, 569 (2000).
[11] M. Yokoyama *et al.*, Nucl. Fusion **40**, 261 (2000).
[12] L. Yao, *New Developments in Nuclear Fusion Research* (Nova Sci. pub, 2006) pp.61-87.
[13] S. Kobayashi *et al.*, J. Plasma Fusion Res. SERIES **9**, 59 (2010).
[14] S. Murakami *et al.*, Trans. Fusion Tech. **27**, 259 (1995).
[15] OPEN-ADAS database, http://open.adas.ac.uk
[16] K.H. Burrell *et al.*, Am. J. Phys. **58**, 2 (1990).
[17] H.C. Burger and H.B. Dorgelo, Z. physik **23**, 258 (1924).